Reconciling remote sensing and reanalysis land surface temperatures: How surface conditions shape systematic differences between GOES-16 and MERRA-2 across the contiguous US

Dhruva Kathuria,[a,b] Alexandra G. Konings,[c] Jana Kolassa,[b,d,e] Yanlan Liu,[f,g] Meng Zhao,[h] Alexey N Shiklomanov[b]

[a] *GESTAR II, Morgan State University, Baltimore, MD*

[b] *Global Modeling and Assimilation Office, NASA Goddard Space Flight Center, Greenbelt, MD*

[c] *Department of Earth System Science, Stanford University, Stanford, CA*

[d] *Science Systems and Applications, Inc., Lanham, MD*

[e] *European Centre for Medium-Range Weather Forecasts, Bonn, Germany*

[f] *School of Environment and Natural Resources, The Ohio State University, Columbus, OH*

[g] *School of Earth Sciences, The Ohio State University, Columbus, OH*

[h] *Department of Earth and Spatial Sciences, University of Idaho, Moscow, ID*

Corresponding author: Dhruva Kathuria, dhruva.kathuria@nasa.gov

ABSTRACT

Land surface temperature (LST) is a key variable governing land–atmosphere energy and water exchanges. Despite the importance of LST, satellite observations and reanalysis products often differ in how they define the effective LST depth and in the assumptions underlying their estimates, making comparisons and interpretation challenging. In this study, we present a detailed comparison of LST from GOES-16 (satellite) and MERRA-2 (reanalysis) across the contiguous United States for 2022 and 2023. The results reveal systematic diurnal and seasonal differences: GOES-16 tends to be warmer than MERRA-2 in the afternoon and at night, but cooler in the morning. The magnitude of these differences varies by season. At night, GOES-16 is warmest relative to MERRA-2 for forests; in the morning, it is coolest for croplands and grasslands; and in the afternoon, it is warmest for barren and shrublands. Within individual land cover types, variability in surface conditions—such as soil moisture and elevation—modulates the differences at night and in the morning, with GOES-16 LST being warmer at night and cooler in the morning for wetter soils and at higher elevations. Our analysis also indicates that Leaf Area Index plays a role during spring and autumn, likely due to the association of temperature with leaf emergence and senescence. These findings provide new insights into the mechanisms underlying LST differences between these datasets, and highlight the importance of accounting for surface condition variability when developing LST fusion and assimilation workflows.

1. Introduction

Land surface temperature (LST) represents the temperature of the top layer of the earth's surface encompassing soil, vegetation or other surface features. As a key variable in land-atmosphere interactions, LST regulates the exchange of energy and water between the surface and the atmosphere (Li et al., 2023; Norman & Becker, 1995). Its significance extends across various disciplines, playing a crucial role in phenology and the carbon cycle (Zhang et al., 2007), soil moisture estimation (Gallego-Elvira et al., 2019; Zhao et al., 2021), evapotranspiration modeling (Kalma et al., 2008), drought monitoring (Karnieli et al., 2010), geology (Watson, 1975), and urban heat island assessment (Peng et al., 2018). Despite its importance, global scale LST

measurements and model products differ in the depths over which LST is averaged and in their underlying assumptions, leading to uncertainties in their comparability and interpretation.

Space-borne remote sensing platforms provide an efficient method to retrieve LST on a global scale. Among them, satellite-borne sensors with thermal infrared channels have demonstrated strong performance in terms of both accuracy and spatiotemporal resolution (Jia et al., 2024). Satellite-derived LST is commonly referred to as skin LST due to its shallow penetration depth (for both soil and vegetation canopy), which typically ranges from 1 to 100 μm. LST retrievals in the thermal infrared region are often performed using semi-empirical algorithms that determine LST as a function of top-of-atmosphere brightness temperatures while incorporating surface emissivity and atmospheric conditions as key constraints (Li et al., 2023). Geostationary satellites, due to their high temporal frequency sampling from 30 seconds to 1 hour, can characterize the LST diurnal temperature curve of a pixel, though at a coarser resolution than orbiting satellites (Freitas et al., 2013). However, satellite-derived LST is affected by cloud contamination (e.g., Figure 1a), which substantially restricts data availability. Alternatively, reanalysis products—which update land surface model states with multi-source observations through data assimilation (Baatz et al., 2021)— provide LST estimates with spatiotemporal continuity in all-weather conditions (Jia et al., 2024). However, this advantage comes at the cost of coarser spatial resolution compared to satellite-based products (e.g., Figure 1b). To maximize the benefits of both satellite-derived and reanalysis-derived LST while mitigating their respective limitations, there has been significant interest in integrating remote sensing observations with reanalysis products through downscaling (Jia et al., 2022) or data fusion/assimilation techniques (Bateni et al., 2013; Caparrini et al., 2003; Dong et al., 2022; Ghent et al., 2010; Lu et al., 2017; Meng et al., 2009; Olivera-Guerra et al., 2025). Such approaches aim to generate all-weather LST datasets and enhance the simulation of water and energy fluxes.

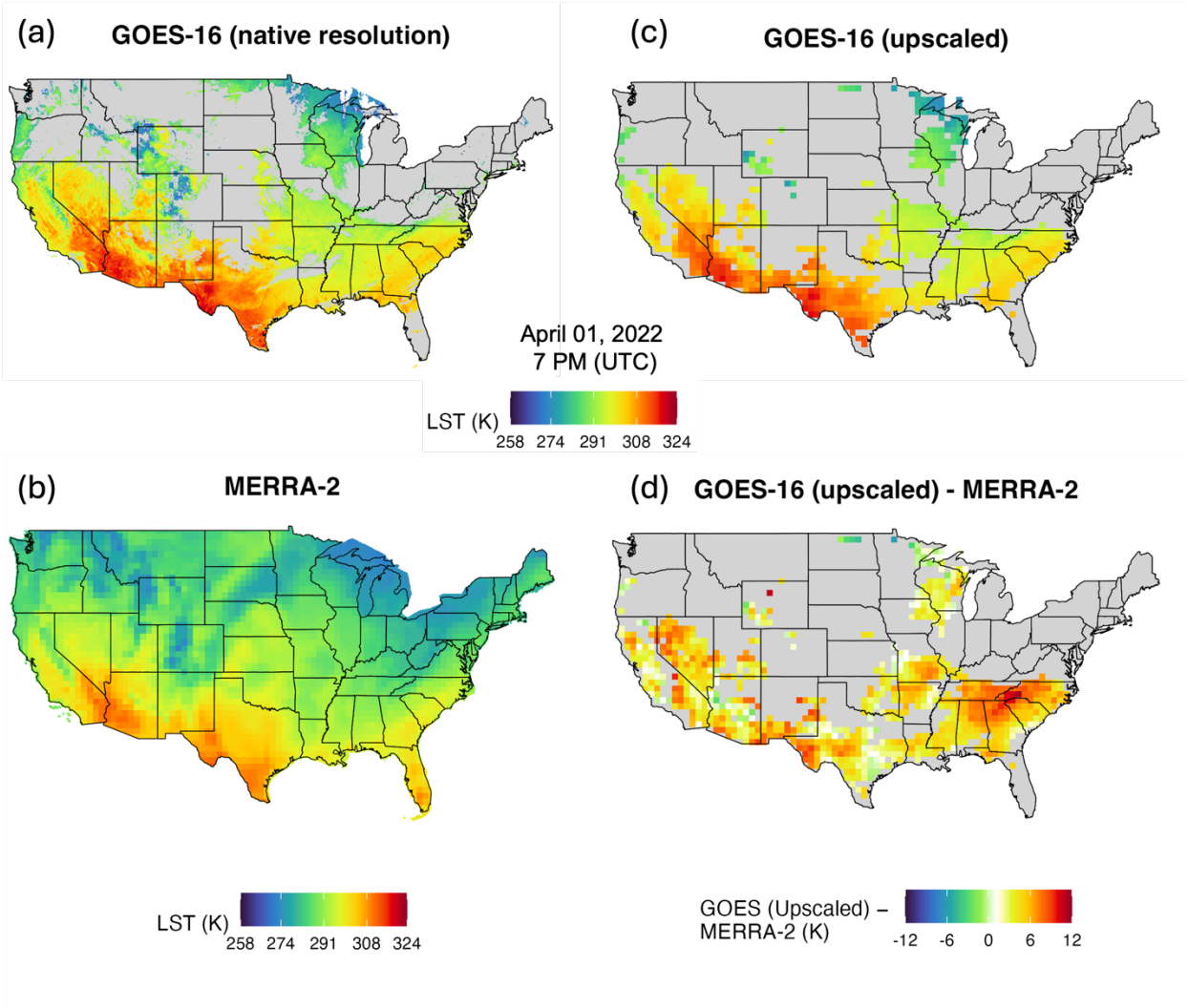

Figure 1. Comparison of land surface temperature (LST) from (a) GOES-16 at its native 2 km resolution and (b) MERRA-2 at approximately 0.625° × 0.5° resolution for 1 April 2022 at 7 PM (UTC). GOES-16 LST is available only under clear-sky conditions and therefore exhibits spatial gaps due to cloud cover, whereas MERRA-2 provides complete spatial coverage at each hourly time step. For each hour, GOES-16 LST is aggregated to the MERRA-2 grid subject to quality constraints (c), and the difference (GOES-16 upscaled − MERRA-2) is computed at the MERRA-2 resolution (d).

Combining these data sources, however, is challenging due to differing modeling assumptions and the strong influence of land surface conditions on both LST satellite retrievals and reanalysis LST estimates. For example, reanalysis-derived skin LST can exhibit systematic differences due to variations in the depth over which LST is averaged, leading to potential discrepancies when compared with in situ measurements or satellite-based LST (Wang et al., 2022). Ancillary data on land cover, elevation, soil texture, Leaf Area Index (LAI), and other surface properties are

important inputs to both reanalysis products and satellite retrieval algorithms, but differences in these input datasets can lead to differences in LST estimates. Land surface heterogeneity also influences thermal infrared LST retrievals: satellite-derived LST can be affected by variations in land cover, vegetation (Guillevic et al., 2013; Inamdar et al., 2008; Lagouarde et al., 2000), soil moisture (Friedl & Davis, 1994; Sun & Pinker, 2004), elevation (Beale et al., 2020; Ma et al., 2021), and soil texture (Müller et al., 2016; Wang et al., 2015). Additionally, thermal infrared LST retrievals depend on surface emissivity—used either as an input or estimated alongside LST—which itself varies with observation viewing angle of the sensor (Ermida et al., 2024; Pérez-Planells et al., 2022) as well as with seasonality, land cover type, soil moisture, soil texture, vegetation density, and vegetation structure (Jin & Liang, 2006; Mira et al., 2010).

Thus, satellite-derived and reanalysis-based LST can differ substantially in their representation of skin LST across times of day, seasons, and varying surface conditions. However, the effects of these conceptual and structural differences remain poorly understood. Examining the spatiotemporal differences between skin LST from satellites and reanalysis products, as well as assessing the influence of land surface conditions on these differences, is a critical step toward improving the interpretation, fusion, and ultimately the assimilation of thermal infrared LST into land surface models. Here, we compare thermal satellite estimates of skin LST from the Geostationary Operational Environmental Satellite-16 (GOES-16; Yu et al. (2012b); Yu & Yu (2020)) to reanalysis estimates of skin LST from the Modern-Era Retrospective Analysis for Research and Applications, version 2 (MERRA-2; Gelaro et al. (2017)). While we expect GOES-16 and MERRA-2 to exhibit broadly consistent spatial and temporal patterns, we anticipate notable differences in magnitude. Specifically, due to its greater representative depth, we hypothesize that MERRA-2 has a more muted and lagged diurnal cycle than GOES-16 does. We expect these systematic differences to be more pronounced in densely vegetated areas because GOES-16 primarily senses the radiometric temperature of the few millimeters of vegetation (with effective sensing depth varying with vegetation density and structure), whereas MERRA-2 represents a “skin” temperature that integrates the entire canopy and the top few cm of soil. Additionally, we expect substantial variations between these datasets in mountainous regions due to the impact of topography on thermal infrared LST retrievals. While previous studies (e.g., Ma et al., 2021) have assessed the accuracy of individual remote sensing and reanalysis LST

products using in situ data, we are not aware of any that have directly compared these datasets to better understand their differences and the role of land surface conditions in shaping them. Furthermore, seasonal effects of surface controls on LST accuracy have not been fully considered. This study aims to address two key questions:

(a) Are there systematic differences between GOES-16 and MERRA-2 LST and, if so, how do they vary across space and time?

(b) Which land surface characteristics are most likely to drive substantial LST differences between GOES-16 and MERRA-2?

2. Study Area

The study area encompasses the contiguous United States, which was selected because GOES-16 LST has been extensively validated across diverse land covers in this region using in situ measurements from the National Oceanic and Atmospheric Administration's (NOAA) Surface Radiation Budget network (SURFRAD; Augustine & Dutton, 2013; Yu et al., 2012b), providing greater confidence in the product's accuracy. Additionally, GOES-16 LST is available at a high resolution of 2 km for the contiguous United States (compared to 10 km for the full disk coverage) (Yu et al., 2012b; Yu & Yu, 2020). The study focuses on four months—January, April, July, and October—for the years 2022 and 2023. These months are assumed to be representative of the winter, spring, summer, and fall seasons, respectively. Conducting the analysis for all months or more than two years was not feasible due to computational constraints. The analysis is restricted to the years 2022 and 2023 because product quality information, critical for filtering out low-quality GOES-16 retrievals, was not available for earlier years at the time of this study.

3. Data

a. MERRA-2 LST

MERRA-2 is the National Aeronautics and Space Administration's (NASA) state-of-the-art reanalysis product, developed by the Global Modeling and Assimilation Office (Gelaro et al., 2017). MERRA-2 provides simulations of skin LST along with various land surface estimates—including soil moisture, streamflow, terrestrial water storage, and snow (Reichle et al., 2017a). While numerous studies have examined the use of MERRA-2 near-surface air temperature (Gupta et al., 2020; Huang et al., 2023) in various applications, the skin LST product remains largely underused by the broader scientific community.

The Catchment Land Surface Model (Koster et al., 2000) governs land surface processes within the MERRA-2 reanalysis framework. This model divides the continental surface into hydrological catchments, varying in size from a few kilometers to approximately 250 km, with the boundaries defined by topography. Each MERRA-2 grid cell (~ $0.625^{o} \times 0.5^{o}$ spatial resolution) contains one or more of these irregularly shaped catchments, and some catchments span multiple MERRA-2 pixels. Each catchment is divided into areas that are either saturated, unsaturated, or wilting, and the fractional areas in each of these states are dynamically adjusted based on the catchment's total water content. The surface energy balance — including LST — is calculated separately for each of these areas, and the skin LST of each MERRA-2 pixel is calculated as an area-weighted average of these LSTs within that pixel. The LST is representative of a composite surface layer with a finite and constant soil layer heat capacity (70,000 J kg^{-1} K^{-1}), encompassing both the vegetation canopy and approximately the top 5 cm of the soil (except for tropical forests; Koster et al. (2020)).

MERRA-2 assimilates a broad range of atmospheric observations, including atmospheric motion vectors, wind speed and wind vector measurements, atmospheric temperature and ozone profiles, and radiance observations from multiple satellite and in situ platforms, including the GOES series. However, MERRA-2 does not directly assimilate land surface observations (Reichle et al., 2017b) including LST. The land surface ancillary datasets used in the current implementation of the Catchment LSM within MERRA-2 include high-resolution elevation data from the Shuttle

Radar Topography Mission (Slater et al., 2006), 1 km soil texture information from De Lannoy et al. (2014), prescribed seasonally varying LAI fields derived from a merged MODIS and Geoland2 dataset (Baret et al., 2013; Camacho et al., 2013), and land cover information from the Globcover v2.3 dataset (GLOBCOVER, 2011). These prescribed surface characteristics influence the model's representation of surface energy and water fluxes and, consequently, the simulated skin LST.

b. GOES-16 LST

Thermal infrared skin LST derived from the Advanced Baseline Imager onboard GOES-16 (Yu et al. (2012b); Yu & Yu (2020); ABI L2+ LST) is available at a 2 km hourly resolution for the contiguous United States and has reached provisional maturity, demonstrating stable accuracy based on ground validation studies (Yu et al., 2012a; Yu & Yu, 2020). The Advanced Baseline Imager in GOES-16 has 16 spectral bands, out of which infrared bands 14 (centered at 11.2 μm) and 15 (centered at 12.3 μm) are used for LST retrieval using the split-window technique (Yu et al., 2008). Assuming we have a good estimate of surface emissivity, the split window technique is a semi-empirical approach that uses the difference between top-of-atmosphere brightness temperature measurements of these two bands to provide an atmospheric correction. The current GOES-16 LST algorithm is based on the split-window formulation proposed by Ulivieri & Cannizzaro (1985) (Eq. 1). This formulation is adopted due to its simplicity and reduced sensitivity of retrieved LST to uncertainties in surface emissivity, atmospheric water vapor, and satellite zenith angle—three of the dominant error sources in split-window LST retrievals.

$$\mathrm{T_s} = \mathrm{C} + \mathrm{A_1 T_{11}} + \mathrm{A_2}(\mathrm{T_{11}} - \mathrm{T_{12}}) + \mathrm{A_3}\epsilon + \mathrm{D}(\mathrm{T_{11}} - \mathrm{T_{12}})(\sec\theta - 1) \quad (1)$$

where T_{11} and T_{12} are top-of-atmosphere brightness for ABI bands 14 and 15 respectively; ϵ_{11} and ϵ_{12} are the corresponding land surface spectral emissivities; $\epsilon = 0.5 * (\epsilon_1 + \epsilon_2)$ is the mean emissivity; θ is the satellite view zenith angle; and C, A_1, A_2, A_3 and D are the algorithm coefficients.

At the time of this analysis, the surface emissivity was derived from the MODIS operational monthly land surface emissivity product (MOD11) based on the methodology described by

Seemann et al. (2008). To account for differences in LST retrievals caused due to atmospheric water content as well as differences in discontinuity between LST and air temperatures during daytime and nighttime, the five algorithm coefficients for the split-window equation have been specified uniquely for four different scenarios: day with dry atmosphere, day with moist atmosphere, night with dry atmosphere, night with moist atmosphere (Yu et al., 2012b; Yu & Yu, 2020). Day–night classification is determined using the solar zenith angle, while dry–moist conditions are identified using total precipitable water retrieved from the GOES-16 Advanced Baseline Imager baseline products. The mission requirements specify an LST accuracy (systematic error) of 2.5 K and a precision (random error) of 2.3 K. The 2.5 K accuracy is conditional on accurate surface emissivity and atmospheric correction, and satisfactory instrument calibration; otherwise, it can increase to 5 K (Yu et al., 2012b).

c. Land surface data

We use 17 land cover classes defined by the International Geosphere-Biosphere Programme (IGBP) based on the Moderate Resolution Imaging Spectroradiometer (MODIS) Land Cover Type product (Friedl & Sulla-Menashe (2022); MCD12Q1, Version 6.1), available at a 500 m spatial resolution. Elevation data are obtained from the Shuttle Radar Topography Mission (Farr & Kobrick (2000); SRTM GL1) at 30 m resolution. Percent clay content is derived from the gridded Soil Survey Geographic database (Staff, 2020), also at 30 m spatial resolution. Additionally, we use MERRA-2 hourly surface soil moisture (5 cm depth) and climatological prescribed LAI fields derived from the Advanced Very High Resolution Radiometer (and provided within the MERRA-2 reanalysis), both at a spatial resolution of 0.625° × 0.5°.

4. Methods

We computed the hourly differences between the two datasets at the spatial resolution of MERRA-2 across the diurnal cycle and averaged them temporally over January, April, July, and October. To assess how surface conditions influence these differences, we analyzed them with respect to five land surface drivers: land cover, LAI, soil moisture, elevation, and clay content (a proxy for soil texture). To interpret these relationships, we first identified the primary driver of LST variability between GOES-16 and MERRA-2— the variable that explains the largest

proportion of spatial variation in their systematic differences. We then examined how the remaining variables contribute to explaining the residual variability.

a. Preprocessing

1. LST DATA

We reproject the GOES-16 LST data from the geostationary satellite view projection to the MERRA-2 WGS84 geographic projection (EPSG: 4326), which requires spatial interpolation. We use bilinear interpolation for LST values and nearest-neighbor interpolation for product quality information flags.

The product quality information includes flags for LST quality, which indicate categories such as no retrieval, low quality, medium quality, and high quality. It also includes flags for land surface type (land, snow/ice, inland water, and coastal) and cloud conditions (clear, probably clear, probably cloudy, and cloudy). We treat inland water pixels as land and generate retrievals over snow/ice. However, most coastal regions (99%) contain no retrievals. To prevent potential errors from including coastal water pixels, we exclude all GOES-16 pixels flagged as coastal from the analysis. The product does not provide retrievals under cloudy conditions. Pixels flagged as low-quality LST are those that meet any of the following conditions: (1) probably cloudy skies, (2) presence of thin cirrus clouds, (3) atmospheric optical depth greater than 1.0, or (4) active fire within the pixel. We exclude all GOES-16 pixels flagged as low-quality LST from the analysis.

We linearly aggregate the GOES-16 pixels to MERRA-2 resolution (e.g., Figure 1c) by assuming that a GOES-16 pixel is entirely contained within a MERRA-2 pixel if its center coordinate lies within the extent of the MERRA-2 pixel. Since the split-window algorithm used by GOES-16 determines LST as a linear function of the brightness temperatures (Yu et al., 2012b; Yu & Yu, 2020), we do not expect that directly aggregating LST values linearly to match the MERRA-2 resolution will introduce significant errors. Direct linear aggregation of satellite-derived LST to the spatial resolution of land surface models has also been commonly employed in previous studies (Ghent et al., 2010; Reichle et al., 2010). To ensure a fair comparison between the two

LST products, we include only those MERRA-2 pixels that contain at least 85% valid GOES-16 LST pixels flagged as medium or high quality and non-coastal. For example, in Figure 1d, the differences between the upscaled GOES-16 LST and MERRA-2 LST are calculated only for the MERRA-2 pixels that meet the criteria described above. This criterion limits the combined contribution of cloudy and probably cloudy pixels to a maximum of 15% of the total MERRA-2 pixel area. We note that the Global Space-based Inter-Calibration System (Goldberg et al., 2011) recommends area-weighted aggregation based on the fractional overlap between high- and low-resolution grids for intercomparison studies. In principle, area-weighted aggregation provides a more exact treatment of partial pixel overlap between the two grids. However, given the large number of GOES-16 pixels within each MERRA-2 grid cell and our requirement that at least 85% of each MERRA-2 pixel be covered by valid GOES-16 retrievals, the contribution of partially overlapping edge pixels is expected to be minimal. Under these conditions, assigning GOES-16 pixels to a MERRA-2 cell based on the pixel center provides a close approximation to area-weighted aggregation and is not expected to significantly influence the results. Both MERRA-2 and GOES-16 data are provided in Coordinated Universal Time (UTC). We perform the diurnal analysis in local time by converting the UTC timestamps to local time, using the center coordinate of each MERRA-2 pixel. Because local time is assigned using the MERRA-2 grid-cell center, small deviations from true solar time may occur, particularly across large time zones. However, given that the analysis employs 3-hour temporal averaging windows (Section 4.b), the influence of these sub-hour timing offsets on the aggregated diurnal statistics is expected to be negligible.

2. LAND SURFACE CONTROLS

We consolidate several land cover classifications into broader composite categories to ensure adequate pixel representation within each group. Specifically, we group cropland and cropland/natural vegetation into a single "cropland" category; closed and open shrublands into "shrubland"; all forest types—evergreen needleleaf, evergreen broadleaf, deciduous needleleaf, deciduous broadleaf, and mixed forest—into "forest"; and woody savannas and savannas into "savanna." We assign 500 m land cover pixels to a MERRA-2 pixel if their center coordinates fall within the MERRA-2 pixel boundary, and compute the fractional coverage of each land cover class within the MERRA-2 pixel. The dominant land cover classification is then defined as

the land cover type occupying at least 50% of the total MERRA-2 pixel area. We exclude MERRA-2 pixels dominated by water, snow and ice, or urban areas, as our analysis focuses on land surface covariates. When analyzing the influence of dominant land cover on LST differences (Section 5.b), we also exclude pixels classified as permanent wetlands due to their limited representation (only three pixels within the contiguous United States). Additionally, we exclude mixed land cover pixels—those where no single land cover type exceeds 50%—from Section 5.b, as their high variability prevents the generalization of LST difference patterns across surface conditions. However, we retain these pixels in the broader analysis in Section 5.a.

For the land cover analysis, we focus on six dominant land cover types: barren land, cropland, forest, grassland, savanna, and shrubland (Figure 4a). In interpreting the results, we combine barren land (38 pixels across contiguous United States) and shrubland (172 pixels) due to predominantly low LAI values for pixels with shrublands as dominant land cover—more than 90% of the shrubland pixels across the two years have an LAI less than 1 representing sparse vegetation cover. For the remaining surface controls—elevation, LAI, soil moisture, and clay content—we compute mean values by applying a linear spatial average at the MERRA-2 spatial resolution.

b. Statistical metrics

Computing pixel-wise systematic differences between two LST datasets is an effective way to assess spatial patterns in their LST differences (e.g., Ma et al., 2021). Such differences may arise from factors such as variations in vertical effective depth and modeling assumptions. We define the systematic difference δ_{G-M} between GOES-16 and MERRA-2 as

$$\delta_{G-M} = \mathrm{E}(\mathrm{LST_G} - \mathrm{LST_M}) \quad (2)$$

where E denotes the expectation, $\mathrm{LST_G}$ represents the upscaled GOES-16 LST for a MERRA-2 pixel, and $\mathrm{LST_M}$ is the corresponding MERRA-2 LST. We calculate this expectation separately for each month and hour by first computing the pixel-wise LST differences between GOES-16 and MERRA-2 for each hour across all available days (subject to quality control constraints in

Section 4.a.1) within a month, and then temporally averaging these differences. We compute δ_{G-M} for a pixel only if it contains data for at least five days for a given hour and month. Although this threshold may appear low, Figure S1 (Supporting Information) shows no significant dependence of δ_{G-M} on the number of available days per month, and most pixels in the analysis contain a higher number of days for each time period. In the land cover analysis (Section 5.b), we spatially average δ_{G-M} for all pixels within a dominant land cover type. In Section 5.c, we do not spatially average δ_{G-M} across pixels; instead, we examine how spatial variability in δ_{G-M} relates to change in land surface controls. For an hour and month, to identify the percent of spatial variability in δ_{G-M} explained by a surface control, we use the one-way Analysis of Variance (ANOVA) for categorical variables (e.g., land cover), and the coefficient of determination for continuous variables (e.g., elevation).

To streamline the discussion, we present our results averaged over three key time periods: night (12 AM–3 AM), morning (8 AM–11 AM), and afternoon (2 PM–5 PM). These time periods were selected because they represent critical phases of the LST diurnal cycle. Additionally, for the selected morning and afternoon periods, the largest diurnal LST differences consistently fell within these intervals across all seasons. We quantify the linear association between a surface control and δ_{G-M} (Section 5.c) using the Pearson correlation coefficient (R). We calculate R for each time period (night, morning and afternoon), month, and land cover type by pooling all pixels across the two study years. For each pixel, we linearly average the corresponding surface control over the selected time interval and month for each year separately, and then correlate the time period specific monthly means with the systematic LST differences. While there is no universal guideline for interpreting the strength of correlation, we classify it as moderate if absolute R is between 0.4 and 0.6, and strong if absolute R exceeds 0.6.

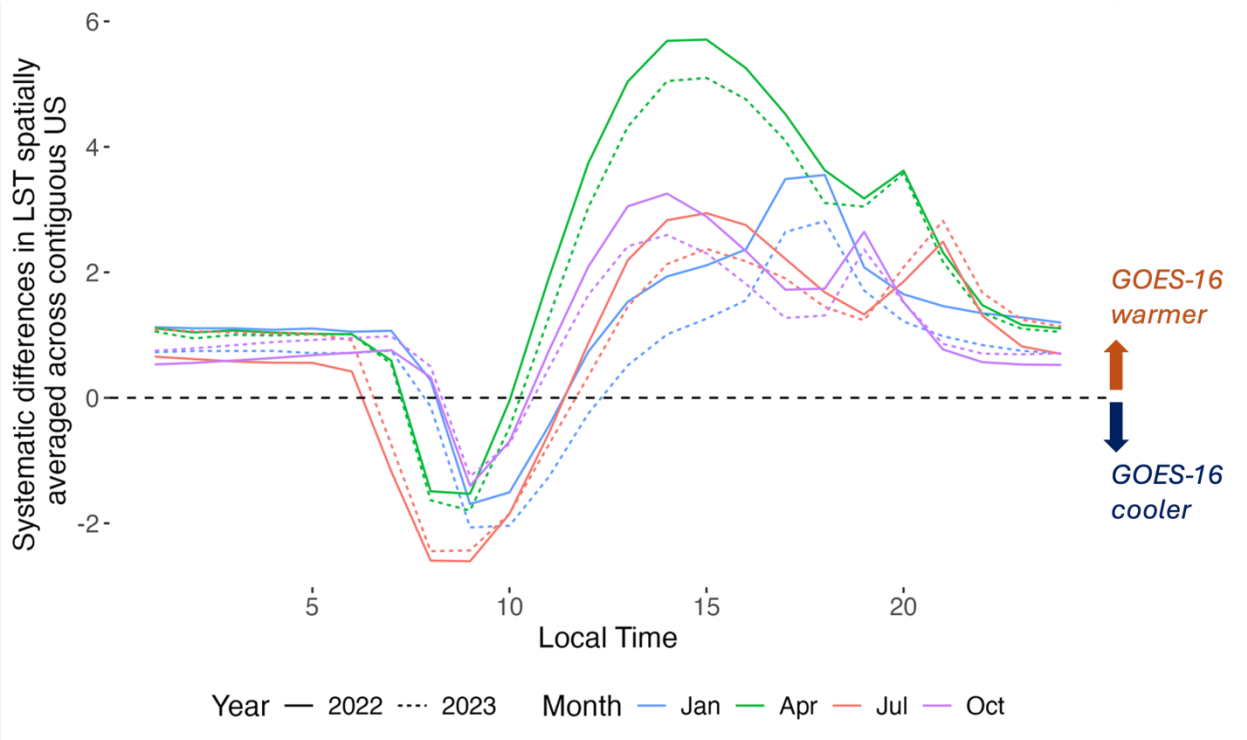

Figure 2. *Spatially averaged systematic differences over the contiguous United States as a function of local time for January, April, July, and October in 2022 (solid lines) and 2023 (dashed lines). Across all months, the diurnal pattern is consistent: GOES-16 is generally warmer than MERRA-2 at night (positive differences), cooler in the morning (negative differences), and substantially warmer in the afternoon, with the magnitude of the afternoon peak varying seasonally.*

5. Results

a. Diurnal and seasonal variation in LST differences

GOES-16 is warmer or cooler than MERRA-2 depending on the time of day. Figure 2 shows the diurnal spatially averaged systematic LST differences across the contiguous United States. Across seasons and years for the entire contiguous United States, GOES-16, on average, is 1 K warmer than MERRA-2 at night, 1 K cooler in the morning, and 3 K warmer in the afternoon. For a given time period, the magnitude of these spatially-averaged LST differences varies across seasons, while year-to-year variability between 2022 and 2023 is relatively minimal (Figure 2).

Morning differences are largest in July (GOES-16 cooler by 2.3 K) and lowest in October (GOES-16 is cooler by 0.5 K) while the afternoon differences are largest in April (GOES-16 is warmer by 5.2 K) and lowest for January (GOES-16 is warmer by 1.8 K). The magnitude of LST differences at night remains similar across seasons.

Spatial variation in LST differences also depends on the time of day and season (Figure 3 and Figure S2; Supporting Information). Figure 3 shows the spatial patterns of these systematic differences for each time period and season. At night, across all seasons, the majority of pixels exhibit LST differences within the ±2 K range, with most pixels showing GOES-16 LST warmer than MERRA-2. A significant proportion of pixels show GOES-16 more than 2 K warmer than MERRA-2, with January (33%) and April (31%) showing the highest percentages of such pixels. The highest spatial variation (standard deviation = 2.7 K) occurs in January while the lowest variation occurs in July (standard deviation = 1.6 K). Regionally, GOES-16 tends to be warmer than MERRA-2 along the west and east coasts, and cooler in the central regions. The mountainous regions in the western United States—including the Rocky Mountains, Colorado Plateau, and Sierra Nevada—show GOES-16 substantially warmer than MERRA-2 in January.

In the morning, most pixels exhibit GOES-16 LST cooler than MERRA-2, with the majority of pixels falling within a ±2 K LST difference for January (59%), April (77%), and October (84%). July shows the highest percentage of pixels (64%) where GOES-16 is cooler than MERRA-2 by at least 2 K. The overall spatial variation in morning LST differences follows a pattern similar to that observed at night, with January exhibiting the highest variation (standard deviation = 2.8 K) and July the lowest (standard deviation = 1.5 K). Morning spatial patterns shift seasonally: GOES-16 is warmer than MERRA-2 in mountainous regions of the western United States in January, while July shows more spatially uniform patterns. In October, the west coast tends to exhibit moderately warmer GOES-16 LST relative to MERRA-2.

In the afternoon, GOES-16 is warmer than MERRA-2 for most pixels across all seasons (Figure S2; Supporting Information). A substantial proportion of pixels exhibit GOES-16 more than 2 K warmer than MERRA-2, with April showing the highest percentage (91%), followed by October (64%). July has the highest spatial variability in afternoon LST differences (standard deviation = 3.7 K) with October having the lowest variability (standard deviation = 1.7 K). Spatially, in

January, GOES-16 is warmer than MERRA-2 across the western, southern, and eastern United States, while the central-northern region tends to have cooler GOES-16 LST. In July, a pronounced east–west gradient emerges: western regions generally exhibit warmer GOES-16 LST relative to MERRA-2, whereas eastern regions show cooler GOES-16 LST.

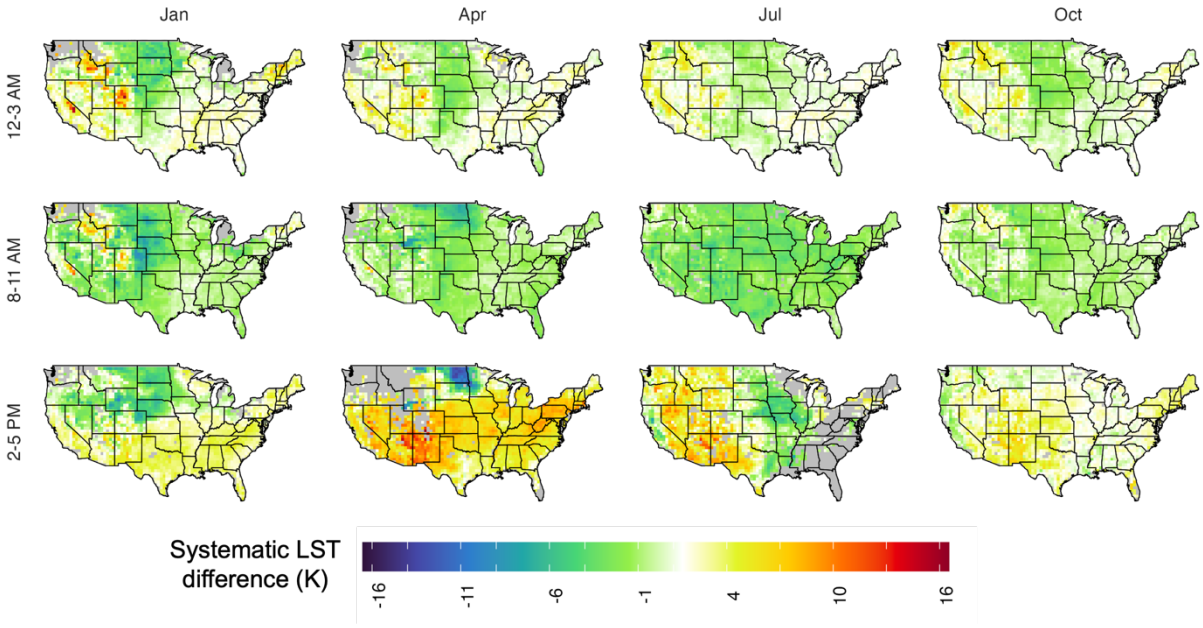

Figure 3. Spatial plots of systematic differences averaged across the two years for three time periods. Across the contiguous United States, the spatial patterns of the systematic differences between GOES-16 and MERRA-2 LST differ substantially across the night (12 AM–3 AM), morning (8 AM–11 AM), and afternoon (2 PM–5 PM) periods, as well as across the four months analyzed. For each time-period and month combination, there are regions where the systematic differences deviate substantially from the spatially-averaged mean shown in Figure 2.

b. Influence of land cover on LST differences

We identify the primary surface driver of systematic LST differences between GOES-16 and MERRA-2 for each hour and month and find that land cover is the dominant driver of these differences across the contiguous United States 78% of the time, explaining an average of 22% of the spatial variation.

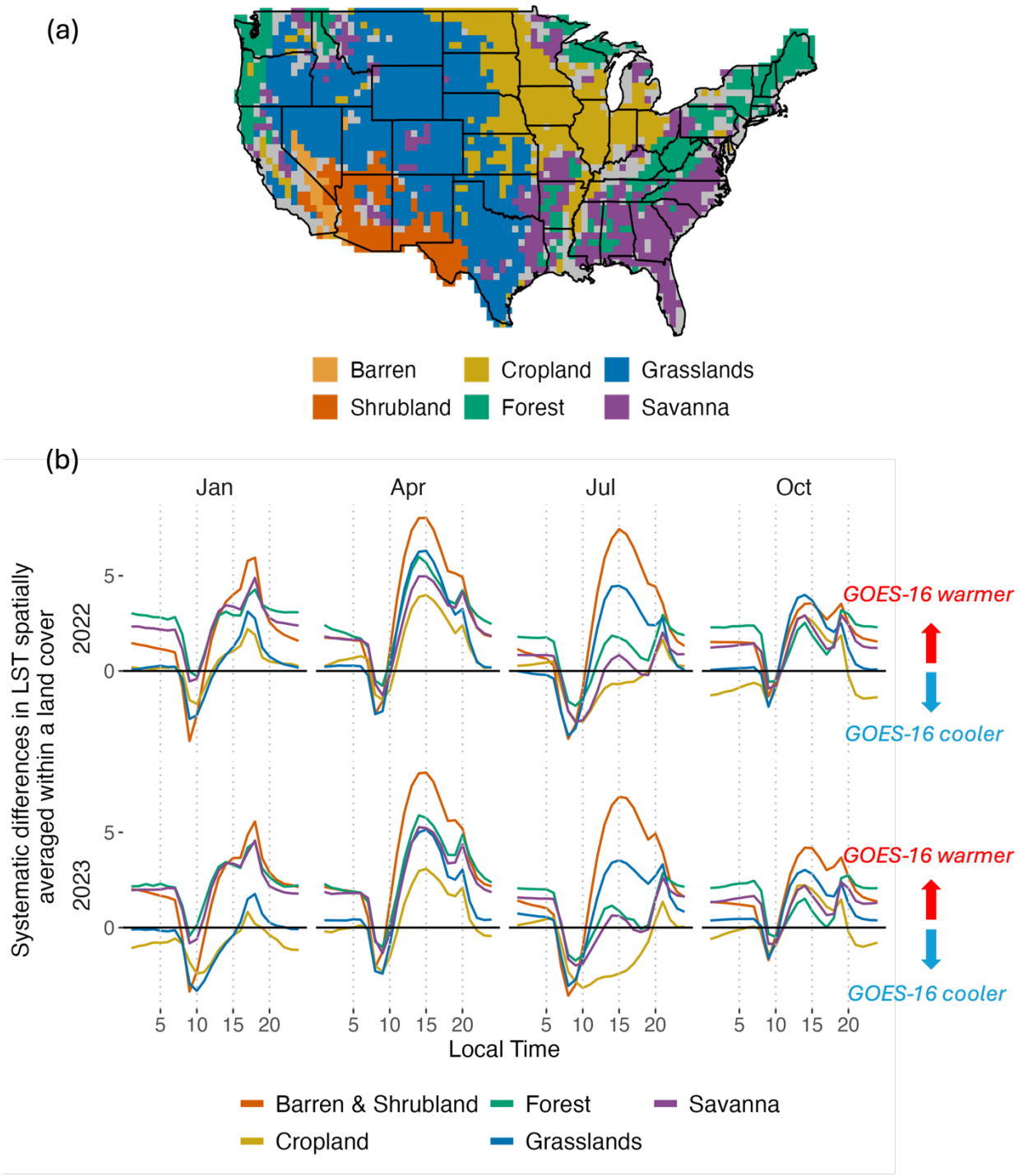

405
406
407 *Figure 4. (a) The six dominant land cover types at MERRA-2 resolution, defined as having at least 50%*
408 *of a specific MODIS 500 m land cover classification within a MERRA-2 pixel, analyzed in this study*
409 *across the contiguous United States. Gray regions indicate pixels where no dominant land cover exists or*
410 *where the dominant land cover is water, snow and ice, or urban areas. (b) For each season, the spatially-*

averaged diurnal systematic differences vary significantly by land cover. At night, GOES-16 is warmest relative to MERRA-2 for forests; in the morning, it is coolest for croplands and grasslands; and in the afternoon, it is warmest for barren and shrublands. Generally, the magnitude of afternoon systematic differences between the two datasets is larger than night. For each month, the diurnal systematic differences shown here are spatially averaged over the respective dominant land cover pixels across the entire contiguous United States.

During the night, forests, savannas, barren areas, and shrublands predominantly exhibit GOES-16 LST warmer than MERRA-2, with a substantial subset of pixels where GOES-16 is warmer by more than 2 K. Figure 4b shows the diurnal spatially averaged systematic LST differences for each dominant land cover type. Among these land cover types, forests exhibit the largest LST differences, with seasonal spatial averages ranging from 1.9 K to 2.7 K and the highest proportion of pixels (34%–67% across the four months) exhibiting GOES-16 more than 2 K warmer than MERRA-2 on average. In contrast, croplands consist of a notable proportion of pixels where GOES-16 LST is cooler than MERRA-2 by at least 2 K, particularly in January (24%), April (18%), and October (21%). Seasonal variability in these differences within individual land cover types is relatively small.

In the morning, across land cover types, most pixels exhibit GOES-16 LST cooler than MERRA-2, except for forests, where more pixels show warmer GOES-16 LST in January (55%) and October (56%). Croplands and grasslands display the highest spatially-averaged LST differences, with GOES-16 cooler than MERRA-2 by 0.8 K to 2.6 K across seasons. For all land covers except forests, variability across land covers in July is relatively small.

During the afternoon, barren and shrubland regions show the highest spatially-averaged LST differences, with GOES-16 warmer than MERRA-2 by 3.8 K to 7.9 K, peaking in April (7.9 K) and followed by July (6.9 K). Croplands record the lowest LST differences; near-neutral in January (0.5 K) and moderate in April (3.3 K). Savannas and forests exhibit smaller differences in July (0.6 K and 1.3 K, respectively) and October (2 K and 1.5 K, respectively). Notably, for croplands in July, GOES-16 is cooler than MERRA-2 by an average of 1.4 K.

Aside from the effect of a pixel's dominant land cover type on the LST differences, we also examined the effect of land cover heterogeneity—defined as the number of distinct land cover

types each occupying at least 10% of the area within a MERRA-2 pixel (Figure 5). After controlling for seasonal and diurnal variability, land cover heterogeneity explains less than 1% of the variance in systematic LST differences, indicating a negligible contribution to the observed LST differences. We further examined the dependence of systematic LST differences on the fractional cover of each land cover class. Relationships between systematic LST differences and fractional land cover (Supporting Information; Figures S3–S7) are weak, seasonally inconsistent, and account for minimal additional variance.

c. Influence of surface conditions on LST differences within land covers

While land cover type is the primary factor contributing to spatial variation in LST differences, significant spatial variability also occurs within individual land cover types. Figure 6 shows the spatial variability of systematic differences between GOES-16 and MERRA-2 LST within each land cover type, with summary statistics provided in Tables S1-S4 (Supporting Information). These variations are largely driven by differing land surface conditions, including soil moisture, elevation, LAI, and clay content, within the same land cover. Figure 7 presents the correlation between these land surface controls and the systematic differences for each time period and season. The influence of these conditions varies depending on the season and time of day, highlighting the dynamic relationship between surface characteristics and patterns of LST differences within a land cover.

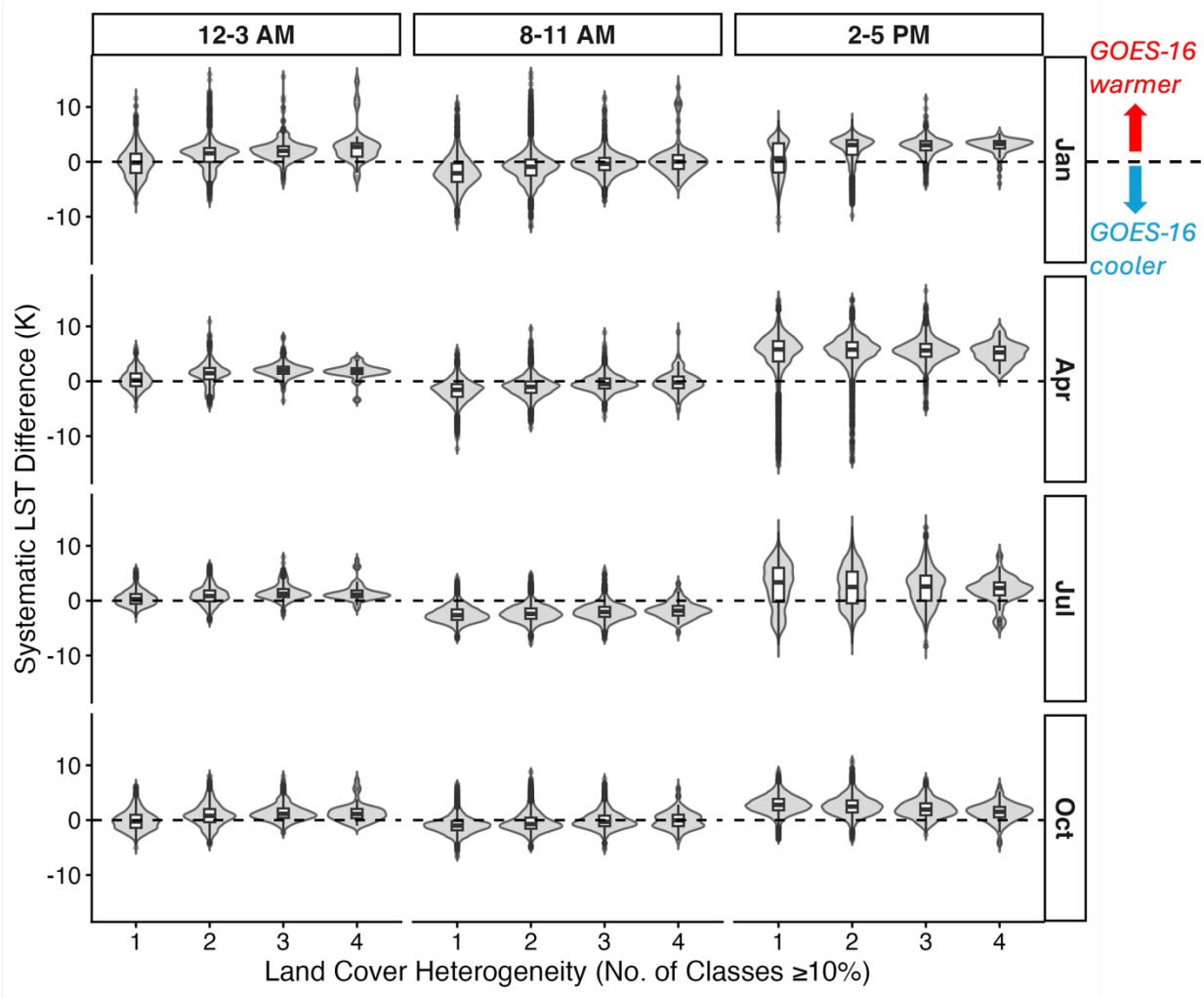

Figure 5. Systematic LST differences as a function of land cover heterogeneity, defined as the number of distinct land cover classes (≥10% area each) within a MERRA-2 pixel. Overall, land cover heterogeneity has a negligible influence on systematic LST differences.

At night, spatial variability in LST differences within land cover types is significantly influenced by elevation and soil moisture. GOES-16 is consistently warmer than MERRA-2 in croplands year-round, with the magnitude of LST differences strongly increasing with soil moisture; in grasslands and in barren and shrubland regions, LST differences moderately increase with soil moisture during the winter and spring months (January and April). Elevation also plays a key role: LST differences increase strongly with elevation in forests (April, July, and October), moderately in grasslands (all months), and moderately to strongly in savannas (all months). In contrast, croplands exhibit a moderate to strong decrease in LST differences with increasing elevation throughout the year. This inverse relationship may be due to the negative correlation

between elevation and soil moisture in croplands (January: -0.72, April: -0.71, July: -0.47, October: -0.37). LAI influence is primarily observed during the fall (October), when LST differences increase strongly with LAI levels in croplands, and moderately in forests and grasslands.

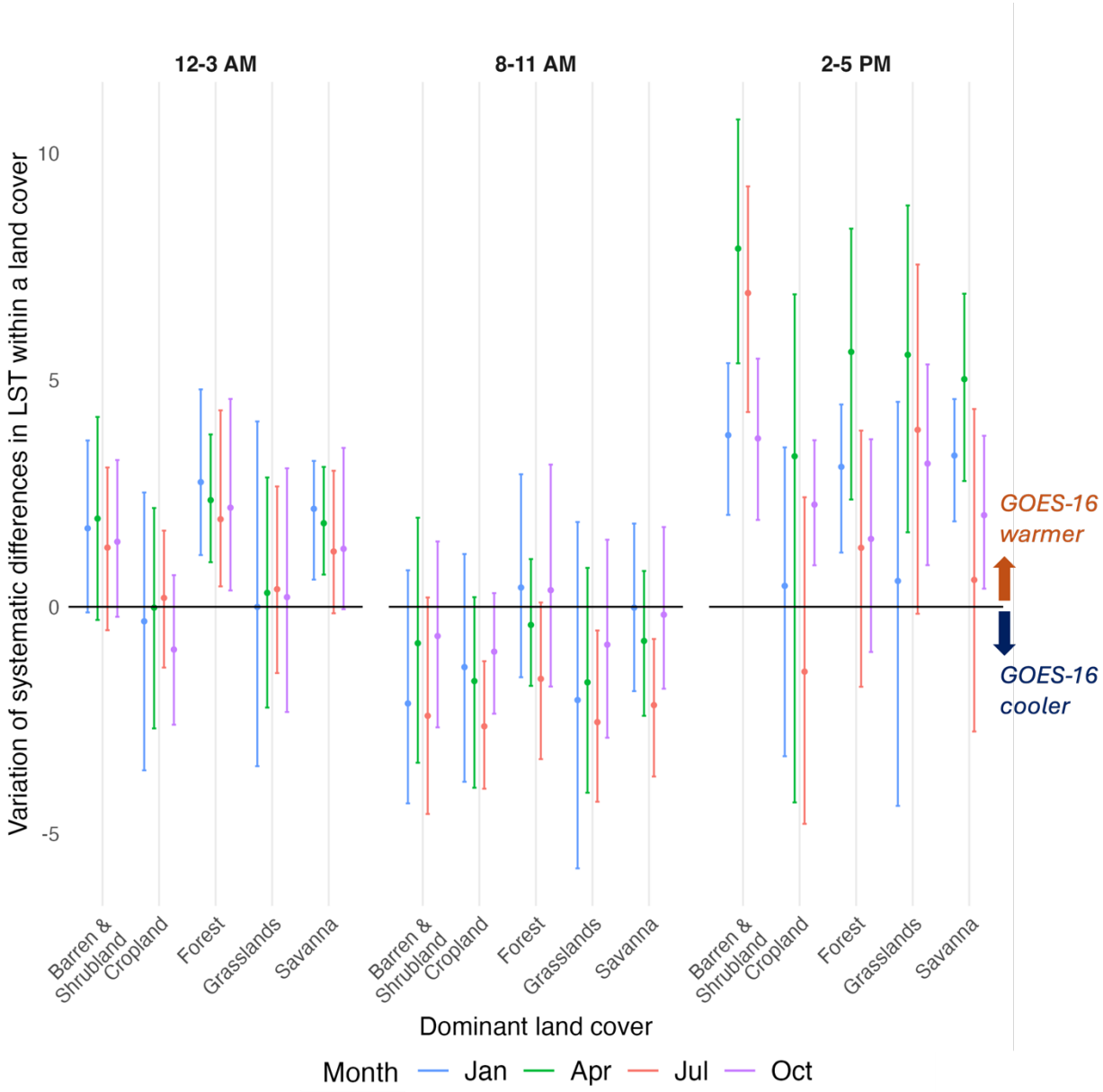

Figure 6. Spatial variation of systematic differences between GOES-16 and MERRA-2 LST within individual land cover types. For each month, time period, and land cover, vertical lines indicate the 10th–90th percentile range of the spatial systematic differences, while filled circles denote the mean. Substantial spatial variability in systematic differences exists within land covers across daily and seasonal timescales.

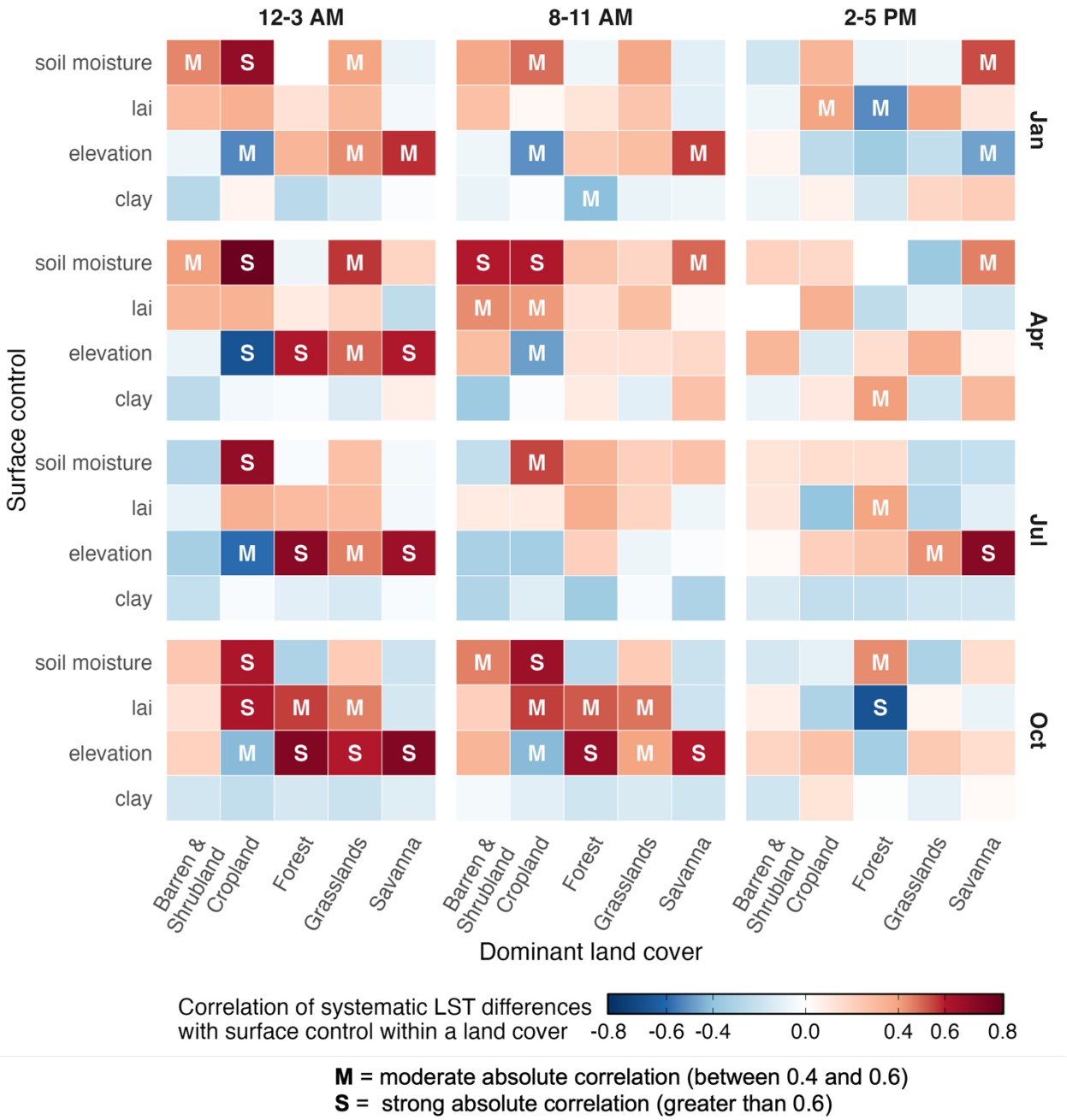

Figure 7. The spatial variability in systematic differences is partly driven by differences in land surface controls within land cover types, including elevation, soil moisture, and Leaf Area Index (LAI). The association of these controls with the systematic differences, quantified using the Pearson correlation coefficient, varies with both time of day and season. We classify the association as moderate when the absolute correlation is between 0.4 and 0.6, and strong when greater than 0.6. At night and in the morning, systematic differences within a land cover are broadly associated with variations in soil moisture, elevation and LAI. By afternoon, the influence of surface controls is generally attenuated.

During the morning, spatial variation in LST differences is most strongly correlated with soil moisture, elevation and LAI. LST differences increase strongly with soil moisture in croplands across all months, and moderately in savannas (April) and in barren and shrubland regions (April and October). With respect to elevation, LST differences increase strongly in forests (October), moderately to strongly in savannas (January and October), and moderately in grasslands (October). Croplands, on the other hand, show a moderate decrease in LST differences with increasing elevation during January, April, and October, which, similar to nighttime patterns, may reflect the negative correlation between elevation and soil moisture (January: -0.74, April: -0.70, October: -0.39). LAI also plays a role, with LST differences moderately increasing with LAI in croplands (April and October), barren and shrubland regions (April), forests (October), and grasslands (October).

The influence of surface covariates on spatial variability in LST differences within a land cover is less pronounced in the afternoon compared to nighttime and morning periods. LAI effects are mixed: in forests, LST differences decrease moderately to strongly in January and October but increase moderately in July; in croplands, LST differences moderately increase with LAI in January. Elevation also plays a role, with LST differences moderately increasing in grasslands and strongly increasing in savannas during July. Unlike the nighttime and morning periods, soil moisture is not the dominant driver of spatial variability in LST differences. However, LST differences moderately increase with soil moisture in savannas (January and April) and forests (October). Supporting Information (Table S5 and Table S6) lists the surface conditions that, for a given time period, month, and land cover, have a high percentage of pixels with an absolute systematic difference greater than 2 K.

We also analyzed the variability of these surface covariates within MERRA-2 pixels, using the standard deviation and coefficient of variation as metrics, but found no significant influence on the LST differences (not shown). Additionally, we compared the prescribed LAI product in MERRA-2 with the observed MODIS LAI product (500 m, 8-day MCD15A2H; (Myneni et al., 2021)) to determine whether pixel-wise differences between the two datasets contributed to LST differences. However, no significant patterns were identified. We conducted a similar comparison between MERRA-2 surface/root-zone soil moisture and the Soil Moisture Active and Passive (SMAP) Level-4 surface/root-zone soil moisture product (Reichle et al., 2018), but

differences between these datasets likewise showed no relationship to LST differences. Furthermore, we investigated whether differences in cloud cover between MERRA-2 and the GOES-16 were associated with consistent patterns in LST differences, but no such patterns were observed.

6. Discussion

a. Mechanisms underlying LST differences between land covers

1. NIGHT

Our results indicate that GOES-16 LST is mostly warmer than MERRA-2 during nighttime across all seasons for barren and shrubland, forests, and savannas. For barren and shrubland pixels, GOES-16 is warmer relative to MERRA-2, despite the expectation that nighttime radiative cooling typically results in cooler surface soil temperatures compared to deeper layers (Campbell & Norman, 1998). Previous validation studies comparing GOES-16 LST data against SURFRAD in situ measurements at desert and shrubland sites reported that GOES-16 exhibited a negative bias (cooler) relative to SURFRAD (Yu et al., 2012b; Yu & Yu, 2020). Considering that MERRA-2 consistently appears cooler than GOES-16—when it would, in fact, be expected to be warmer due to GOES-16's established negative bias and MERRA-2 being representative of a deeper layer—our analysis suggests that MERRA-2 likely possesses a substantial negative bias at barren and shrubland locations during night relative to the true LST.

In densely forested regions in forests and savannas, GOES-16 LST primarily represents the canopy top, while MERRA-2 calculates LST based on the entire canopy depth and the top few centimeters of soil. Typically, forest canopies cool radiatively by emitting longwave radiation toward both the sky and the ground, resulting in a cooler canopy top relative to deeper canopy layers and underlying soil (Still et al., 2021), although some exceptions exist in colder climates (Staebler & Fitzjarrald, 2005). Contrary to expectations, our findings reveal that GOES-16 LST is warmer compared to MERRA-2. We speculate that one possible explanation for this is that critical biotic and abiotic factors influencing canopy energy balance—e.g., leaf size, clumping, stomatal conductance, canopy structure and function (N. Dong et al., 2017; Jiang et al., 2019;

Still et al., 2021)— are not explicitly represented in the Catchment Land Surface Model. The absence of these factors may influence simulated energy partitioning in forests, potentially contributing to cooler modeled LST relative to GOES-16. However, targeted process-level analyses are required to confirm this hypothesis. This discrepancy is muted in croplands and grasslands.

2. MORNING

Since GOES-16 generally records warmer temperatures at night (except over croplands and grasslands), we expected GOES-16 to also be warmer than MERRA-2 during the morning period, given that the upper few millimeters of vegetation and soil typically warm faster than deeper subsurface layers during the morning (Campbell & Norman, 1998). However, our analysis reveals an opposite trend: GOES-16 is, on average, cooler than MERRA-2 during morning hours, except over forests in January and October, where it is warmer. Several potential factors might explain these observations.

First, GOES-16 observes the contiguous United States at varying viewing angles, potentially altering the proportions of visible soil and vegetation fractions, thereby affecting the retrieved LST. Recent analysis by Qin et al. (2025) using AmeriFlux sites indicated that GOES-16 morning LST retrievals exhibit higher root mean square errors compared to noontime retrievals, primarily due to sun-sensor geometry effects. They demonstrated that explicitly accounting for these angular variations significantly reduces errors. Second, the morning period corresponds to a longer atmospheric optical path length, increasing susceptibility to atmospheric absorption and emission of infrared radiation. Specifically, Pestana et al. (2024) demonstrated that atmospheric absorption in midlatitude winter conditions could make the GOES-R Advanced Baseline Imager surface brightness temperature as much as 4 Kelvin colder than the true surface brightness temperature.

Conversely, for forests, where GOES-16 is typically warmer than MERRA-2 in January and October, prior studies suggest that this discrepancy arises from GOES-16 preferentially observing sunlit portions of trees (Pestana et al. (2024). This effect is most pronounced during

winter mornings (and to a lesser extent in fall), when the angular difference between satellite viewing direction and solar illumination is small for the contiguous United States. At off-nadir angles, GOES-16 captures tree profiles rather than only the canopy top, and tree trunks exposed to insolation can become substantially hotter than other parts of the canopy and the surrounding canopy air temperature (Rutter et al., 2023), especially under sparse canopy conditions (Pomeroy et al., 2009) common in fall and winter. Additionally, for pixels containing forests and snow, trees can obscure the snow surface beneath and behind them (Pestana et al., 2019), causing GOES-16 LST to appear warmer than the actual surface. Consequently, our findings emphasize the importance of incorporating improved angular radiometric corrections and explicitly accounting for enhanced warming in sunlit forested areas when comparing GOES-16 and MERRA-2 LST data during morning periods.

3. AFTERNOON

In general, GOES-16 is substantially warmer than MERRA-2 in the afternoon. This can be attributed to several factors, including uneven solar heating driven by variations in sun-sensor geometry, surface topography, and thermal inertia; and increased thermal emission from exposed surfaces such as rocks and vegetation (Kuenzer & Dech, 2013) during the day. Across all seasons, GOES-16 consistently reports higher LSTs than MERRA-2 over barren lands and shrublands, with the largest discrepancies observed during the months of April and July. We hypothesize that this arises primarily from three factors. First, in dry sparsely vegetated regions, vertical temperature gradients within the soil column become more pronounced, with the top few millimeters substantially warmer than the underlying 5 cm layer (Holmes et al., 2008). Second, daytime LST retrievals over bare soil are more susceptible to errors related to surface emissivity variability than those over vegetated surfaces (Cheng & Liang, 2014; Jin & Liang, 2006; Ogawa et al., 2003). In addition, while directional effects of solar radiation on GOES-16 LST retrievals are generally reduced in the afternoon compared to the morning, these effects tend to be more prominent over sparsely vegetated areas (Carlson et al., 1995).

For croplands, the systematic differences between GOES-16 and MERRA-2 LST are generally lower, particularly in April and July, likely due to frequent irrigation. We hypothesize that this is

related to the increased thermal conductivity of wet soils, which reduces vertical temperature gradients near the surface. In July—when irrigation volumes are typically high due to elevated temperatures—GOES-16 is cooler than MERRA-2 during the afternoon. This may be attributed to the top few millimeters of the soil being significantly cooler than deeper layers due to irrigation-induced effects (Zhu & Burney, 2022). Another contributing factor is that the MERRA-2 Catchment Land Surface Model does not explicitly model irrigation. Additionally, Li et al. (2021) found that GOES-16 LST consistently underestimated LST compared with in situ observations for croplands in the United States corn belt for midday time periods (10 AM–2 PM) which might also explain low systematic differences for croplands between GOES-16 and MERRA-2.

Grasslands exhibit pronounced afternoon LST differences during April and July, which generally correspond to the active growing season. By October, most grasslands enter senescence, while January represents the dormant phase with minimal vegetation activity across the United States (Fischer et al., 2023; Hartman et al., 2020). Accordingly, afternoon LST differences are highest in April and July, lower in October, and negligible in January. We speculate that—in addition to seasonal variations in solar geometry and associated changes in incoming solar radiation—the presence and growth stage of grasslands might also influence the observed LST differences between the two datasets, with larger differences occurring as grassland height and biomass increase. Our analysis indicates that the top few millimeters of the grassland canopy are significantly warmer than the combined grassland canopy and upper 5 cm of soil. This temperature difference appears to amplify during the growing season, decrease during senescence in the fall, and become negligible during dormancy in January. However, additional research is required to evaluate this interpretation.

Forests and savannas exhibit warmer GOES-16 temperatures during the afternoon; this is partly because GOES-16 senses only the top few millimeters of the canopy, which can be warmer than the deeper canopy layers. However, the magnitude of the LST differences between the two datasets varies seasonally. One possible explanation is that canopy structure strongly influences radiative transfer; in heterogeneous canopies, lower leaves can absorb radiation scattered from the upper layers (Roberts et al., 2004; Still et al., 2021). Additional factors such as leaf angle

distribution and clumping also modulate within-canopy radiation absorption. In a forest, canopy temperature itself can vary considerably among species during the day (Zakrzewska et al., 2022). These results are supported by the strong impact of canopy structure representations on LST estimates in land surface models.

b. Influence of surface controls

During the night and morning periods, our results indicate that spatial variability in LST differences within certain land covers—particularly croplands, and to a lesser extent, barren and shrublands and grasslands—is strongly influenced by surface soil moisture. In these regions, higher soil moisture levels are associated with GOES-16 LST being warmer than MERRA-2. One possible explanation is that the MERRA-2 soil moisture product, which we use in this study, represents an effective depth of 5 cm. This depth may not capture the wetness of the top few millimeters that directly influence GOES-16 LST, leading to differences between the two datasets under wetter conditions. Notably, the influence of soil moisture on this spatial variability becomes minimal in the afternoon, suggesting that at the MERRA-2 spatial resolution, vertical LST gradients within individual land cover types are less sensitive to surface soil moisture under high solar insolation, likely because the soil column dries more uniformly with depth as the day progresses. In croplands, an additional factor may be the effect of irrigation: increased soil moisture from irrigation is not explicitly represented in the MERRA-2 Catchment Land Surface Model, potentially contributing to larger discrepancies between the two products at night and morning under wetter conditions, which are more likely to represent irrigated conditions than dry soil moisture levels are.

Elevation plays a significant role in modulating spatial variability in LST differences within forests, savannas, and grasslands at night, while its influence is comparatively minor during the morning and afternoon. Our analysis shows that higher elevations are associated with GOES-16 LSTs being warmer than MERRA-2 during the night. Thermal infrared LST retrievals are known to have high errors in high-elevation regions with rugged topography due to pronounced surface heterogeneity and the effects of viewing geometry (Beale et al., 2020; Jia et al., 2023). Interestingly, compared to daytime thermal infrared LST retrieval errors, our results show that

the effect of elevation on nighttime LST differences is more pronounced. This suggests that these differences are not solely due to insolation contrasts between sunny and shady slopes in mountainous regions, but also reflect the ways in which topography fundamentally alters water, energy, and biogeochemical processes (Hao et al., 2022). For instance, topography significantly influences lateral ridge-to-valley water transport (Fan et al., 2019), and north- and south-facing slopes often support different vegetation types, densities, and species compositions (Dearborn & Danby, 2017)—features that are generally poorly represented in land surface model parameterizations, including the Catchment Land Surface Model. Given that both GOES-16 and MERRA-2 exhibit limitations in high-elevation regions—particularly in complex terrain such as the Rocky Mountains, Colorado Plateau, and Sierra Nevada (as noted in Section 5.a)—our findings underscore the need to improve both satellite-based retrieval algorithms and LST modeling to better capture topography-driven variability in LST.

Interestingly, contrary to our initial hypothesis, the effect of LAI within land cover types is less pronounced. Specifically, the effect of LAI on LST differences appears mainly during the night and morning hours of the spring and autumn seasons. We hypothesize that this seasonal pattern is largely due to the influence of temperature in controlling the onset of the growing season in spring and the timing of senescence in autumn. Multiple studies have shown that variability in temperature strongly affects the timing of leaf-out in spring and senescence in autumn (Gill et al., 2015; Linderholm, 2006; Polgar & Primack, 2011). Land surface models have generally struggled to capture this interannual variability in phenological transition dates and related vegetation processes (Richardson et al., 2012). MERRA-2, which uses prescribed climatological LAI, cannot capture this variability, and this limitation may help explain why the influence of LAI is stronger during transitional seasons than in winter or summer.

7. Conclusion

This study provides a detailed evaluation of diurnal and seasonal LST differences between satellite-derived (GOES-16) and reanalysis-based (MERRA-2) LST across the contiguous United States, with particular emphasis on the role of land surface conditions in shaping these discrepancies. Our results show that GOES-16 is typically warmer than MERRA-2 at night and

during the afternoon, and cooler in the morning. These patterns are primarily attributable to differences in averaging depth between thermal infrared LST retrievals and reanalysis LST estimates, further modulated by soil moisture, elevation, and LAI.

We identify land cover type as the dominant driver of LST differences between the two datasets, which explains a substantial portion of the spatial variability between the two datasets. At night, GOES-16 is significantly warmer than MERRA-2 for forests and savannas, whereas in the morning it is significantly cooler over croplands. During the afternoon, GOES-16 is significantly warmer over barren and shrubland areas, likely driven by shallow surface heating and surface emissivity variability. Within individual land cover types, elevation and soil moisture exert strong controls on nighttime and morning LST differences, while vegetation phenology has a marked influence during transitional seasons (spring and autumn). By contrast, the role of surface controls in the afternoon is comparatively weaker due to the overriding effects of solar insolation.

Our findings underscore key limitations of both GOES-16 thermal infrared LST retrievals and MERRA-2 reanalysis in capturing sub-grid heterogeneity, complex canopy structures, and the influence of irrigation and topography on LST. Addressing these challenges—through improved angular corrections in thermal infrared LST retrieval algorithms, dynamic vegetation parameterizations in land surface models, and enhanced representation of sub-grid surface heterogeneity—will be essential for effectively integrating satellite and reanalysis LST products in environmental applications, hydrological modeling, and numerical weather prediction. Ultimately, this work underscores that effectively reconciling remote sensing and reanalysis-based LST estimates requires capturing the evolving interplay among land cover, surface properties, and effective LST depth, which shifts markedly across the diurnal cycle and seasons.

Acknowledgments

The authors were supported by a NASA Modeling, Analysis, and Prediction grant (80NSSC21K1523). AGK was also supported by the Alfred P. Sloan Foundation. We would also like to thank Rolf H. Reichle for his valuable inputs. The authors declare no conflict of interest.

Data Availability Statement

The LST data used in this study were accessed from www.ncei.noaa.gov/airs-web and https://disc.gsfc.nasa.gov/datasets/M2T1NXRAD_5.12.4/summary?keywords=MERRA-2%20tavg1_2d_rad_Nx. The land cover and elevation data were accessed from https://appeears.earthdatacloud.nasa.gov. The percent clay data was accessed from https://www.nrcs.usda.gov/resources/data-and-reports/gridded-soil-survey-geographic-gssurgo-database.

References

Augustine, J. A., & Dutton, E. G. (2013). Variability of the surface radiation budget over the United States from 1996 through 2011 from high-quality measurements. *Journal of Geophysical Research: Atmospheres*, *118*(1), 43–53. https://doi.org/10.1029/2012JD018551

Baatz, R., Hendricks Franssen, H. J., Euskirchen, E., Sihi, D., Dietze, M., Ciavatta, S., Fennel, K., Beck, H., De Lannoy, G., Pauwels, V. R. N., Raiho, A., Montzka, C., Williams, M., Mishra, U., Poppe, C., Zacharias, S., Lausch, A., Samaniego, L., Van Looy, K., … Vereecken, H. (2021). Reanalysis in Earth System Science: Toward Terrestrial Ecosystem Reanalysis. *Reviews of Geophysics*, *59*(3), e2020RG000715. https://doi.org/10.1029/2020RG000715

Baret, F., Weiss, M., Lacaze, R., Camacho, F., Makhmara, H., Pacholcyzk, P., & Smets, B. (2013). GEOV1: *LAI* and *FAPAR* essential climate variables and *FCOVER* global time series capitalizing over existing products. Part1: Principles of development and

production. *Remote Sensing of Environment*, *137*, 299–309. https://doi.org/10.1016/j.rse.2012.12.027

Bateni, S. M., Entekhabi, D., & Jeng, D.-S. (2013). Variational assimilation of land surface temperature and the estimation of surface energy balance components. *Journal of Hydrology*, *481*, 143–156. https://doi.org/10.1016/j.jhydrol.2012.12.039

Beale, C., Norouzi, H., Sharifnezhadazizi, Z., Bah, A. R., Yu, P., Yu, Y., Blake, R., Vaculik, A., & Gonzalez-Cruz, J. (2020). Comparison of Diurnal Variation of Land Surface Temperature From GOES-16 ABI and MODIS Instruments. *IEEE Geoscience and Remote Sensing Letters*, *17*(4), 572–576. IEEE Geoscience and Remote Sensing Letters. https://doi.org/10.1109/LGRS.2019.2930174

Camacho, F., Cernicharo, J., Lacaze, R., Baret, F., & Weiss, M. (2013). GEOV1: LAI, FAPAR essential climate variables and FCOVER global time series capitalizing over existing products. Part 2: Validation and intercomparison with reference products. *Remote Sensing of Environment*, *137*, 310–329. https://doi.org/10.1016/j.rse.2013.02.030

Campbell, G. S., & Norman, J. M. (1998). Temperature. In G. S. Campbell & J. M. Norman (Eds.), *An Introduction to Environmental Biophysics* (pp. 15–36). Springer New York. https://doi.org/10.1007/978-1-4612-1626-1_2

Caparrini, F., Castelli, F., & Entekhabi, D. (2003). Mapping of Land-Atmosphere Heat Fluxes and Surface Parameters with Remote Sensing Data. *Boundary-Layer Meteorology*, *107*(3), 605–633. https://doi.org/10.1023/A:1022821718791

Carlson, T. N., Taconet, O., Vidal, A., Gillies, R. R., Olioso, A., & Humes, K. (1995). An overview of the workshop on thermal remote sensing held at La Londe les Maures, France, September 20–24, 1993. *Agricultural and Forest Meteorology, Thermal Remote Sensing of the Energy and Water Balance over Vegetation*, *77*(3), 141–151. https://doi.org/10.1016/0168-1923(95)02258-Y

Cheng, J., & Liang, S. (2014). Estimating the broadband longwave emissivity of global bare soil from the MODIS shortwave albedo product. *Journal of Geophysical Research: Atmospheres*, *119*(2), 614–634. https://doi.org/10.1002/2013JD020689

De Lannoy, G. J. M., Koster, R. D., Reichle, R. H., Mahanama, S. P. P., & Liu, Q. (2014). An updated treatment of soil texture and associated hydraulic properties in a global land modeling system. *Journal of Advances in Modeling Earth Systems*, *6*(4), 957–979. https://doi.org/10.1002/2014MS000330

Dearborn, K. D., & Danby, R. K. (2017). Aspect and slope influence plant community composition more than elevation across forest–tundra ecotones in subarctic Canada. *Journal of Vegetation Science*, *28*(3), 595–604. https://doi.org/10.1111/jvs.12521

Dong, N., Prentice, I. C., Harrison, S. P., Song, Q. H., & Zhang, Y. P. (2017). Biophysical homoeostasis of leaf temperature: A neglected process for vegetation and land-surface modelling. *Global Ecology and Biogeography*, *26*(9), 998–1007. https://doi.org/10.1111/geb.12614

Dong, S., Cheng, J., Shi, J., Shi, C., Sun, S., & Liu, W. (2022). A Data Fusion Method for Generating Hourly Seamless Land Surface Temperature from Himawari-8 AHI Data. *Remote Sensing*, *14*(20), Article 20. https://doi.org/10.3390/rs14205170

Ermida, S. L., Hulley, G., & Trigo, I. F. (2024). Introducing emissivity directionality to the temperature-emissivity separation algorithm. *Remote Sensing of Environment*, *311*, 114280. https://doi.org/10.1016/j.rse.2024.114280

Fan, Y., Clark, M., Lawrence, D. M., Swenson, S., Band, L. E., Brantley, S. L., Brooks, P. D., Dietrich, W. E., Flores, A., Grant, G., Kirchner, J. W., Mackay, D. S., McDonnell, J. J., Milly, P. C. D., Sullivan, P. L., Tague, C., Ajami, H., Chaney, N., Hartmann, A., … Yamazaki, D. (2019). Hillslope Hydrology in Global Change Research and Earth System Modeling. *Water Resources Research*, *55*(2), 1737–1772. https://doi.org/10.1029/2018WR023903

809 Farr, T. G., & Kobrick, M. (2000). Shuttle Radar Topography Mission produces a wealth of data.
810 *Eos, Transactions American Geophysical Union*, *81*(48), 583–585.
811 Fischer, F. M., Chytrý, K., Chytrá, H., Chytrý, M., & Těšitel, J. (2023). Seasonal beta-diversity of
812 dry grassland vegetation: Divergent peaks of above-ground biomass and species
813 richness. *Journal of Vegetation Science*, *34*(2), e13182.
814 https://doi.org/10.1111/jvs.13182
815 Freitas, S. C., Trigo, I. F., Macedo, J., Barroso, C., Silva, R., & Perdigão, R. (2013). Land
816 surface temperature from multiple geostationary satellites. *International Journal of*
817 *Remote Sensing*, *34*(9–10), 3051–3068. https://doi.org/10.1080/01431161.2012.716925
818 Friedl, M. A., & Davis, F. W. (1994). Sources of variation in radiometric surface temperature
819 over a tallgrass prairie. *Remote Sensing of Environment*, *48*(1), 1–17.
820 https://doi.org/10.1016/0034-4257(94)90109-0
821 Friedl, M., & Sulla-Menashe, D. (2022). MODIS/Terra+ Aqua land cover type yearly L3 Global
822 0.05 Deg CMG V061. *NASA EOSDIS Land Processes Distributed Active Archive Center*
823 *(DAAC) Data Set*, MCD12C1-061.
824 Gallego-Elvira, B., Taylor, C. M., Harris, P. P., & Ghent, D. (2019). Evaluation of Regional-Scale
825 Soil Moisture-Surface Flux Dynamics in Earth System Models Based on Satellite
826 Observations of Land Surface Temperature. *Geophysical Research Letters*, *46*(10),
827 5480–5488. https://doi.org/10.1029/2019GL082962
828 Gelaro, R., McCarty, W., Suárez, M. J., Todling, R., Molod, A., Takacs, L., Randles, C. A.,
829 Darmenov, A., Bosilovich, M. G., Reichle, R., Wargan, K., Coy, L., Cullather, R., Draper,
830 C., Akella, S., Buchard, V., Conaty, A., Silva, A. M. da, Gu, W., … Zhao, B. (2017). *The*
831 *Modern-Era Retrospective Analysis for Research and Applications, Version 2 (MERRA-*
832 *2)*. https://doi.org/10.1175/JCLI-D-16-0758.1
833 Ghent, D., Kaduk, J., Remedios, J., Ardö, J., & Balzter, H. (2010). Assimilation of land surface
834 temperature into the land surface model JULES with an ensemble Kalman filter. *Journal*

of Geophysical Research: Atmospheres, *115*(D19). https://doi.org/10.1029/2010JD014392

Gill, A. L., Gallinat, A. S., Sanders-DeMott, R., Rigden, A. J., Short Gianotti, D. J., Mantooth, J. A., & Templer, P. H. (2015). Changes in autumn senescence in northern hemisphere deciduous trees: A meta-analysis of autumn phenology studies. *Annals of Botany*, *116*(6), 875–888. https://doi.org/10.1093/aob/mcv055

GLOBCOVER. (2011). *GLOBCOVER 2009, Products Description and Validation Report.* (ESA Technical Note). https://due.esrin.esa.int/files/GLOBCOVER2009_Validation_Report_2.2.pdf

Goldberg, M., Ohring, G., Butler, J., Cao, C., Datla, R., Doelling, D., Gärtner, V., Hewison, T., Iacovazzi, B., Kim, D., Kurino, T., Lafeuille, J., Minnis, P., Renaut, D., Schmetz, J., Tobin, D., Wang, L., Weng, F., Wu, X., … Zhu, T. (2011). The Global Space-Based Inter-Calibration System. *Bulletin of the American Meteorological Society*, *92*(4), 467–475. https://doi.org/10.1175/2010BAMS2967.1

Guillevic, P. C., Bork-Unkelbach, A., Göttsche, F. M., Hulley, G., Gastellu-Etchegorry, J.-P., Olesen, F. S., & Privette, J. L. (2013). Directional Viewing Effects on Satellite Land Surface Temperature Products Over Sparse Vegetation Canopies—A Multisensor Analysis. *IEEE Geoscience and Remote Sensing Letters*, *10*(6), 1464–1468. IEEE Geoscience and Remote Sensing Letters. https://doi.org/10.1109/LGRS.2013.2260319

Gupta, P., Verma, S., Bhatla, R., Chandel, A. S., Singh, J., & Payra, S. (2020). Validation of Surface Temperature Derived From MERRA-2 Reanalysis Against IMD Gridded Data Set Over India. *Earth and Space Science*, *7*(1), e2019EA000910. https://doi.org/10.1029/2019EA000910

Hao, D., Bisht, G., Huang, M., Ma, P.-L., Tesfa, T., Lee, W.-L., Gu, Y., & Leung, L. R. (2022). Impacts of Sub-Grid Topographic Representations on Surface Energy Balance and Boundary Conditions in the E3SM Land Model: A Case Study in Sierra Nevada. *Journal*

of Advances in Modeling Earth Systems, *14*(4), e2021MS002862. https://doi.org/10.1029/2021MS002862

Hartman, M. D., Parton, W. J., Derner, J. D., Schulte, D. K., Smith, W. K., Peck, D. E., Day, K. A., Del Grosso, S. J., Lutz, S., Fuchs, B. A., Chen, M., & Gao, W. (2020). Seasonal grassland productivity forecast for the U.S. Great Plains using Grass-Cast. *Ecosphere*, *11*(11), e03280. https://doi.org/10.1002/ecs2.3280

Holmes, T. R. H., Owe, M., De Jeu, R. A. M., & Kooi, H. (2008). Estimating the soil temperature profile from a single depth observation: A simple empirical heatflow solution. *Water Resources Research*, *44*(2). https://doi.org/10.1029/2007WR005994

Huang, L., Fang, X., Zhang, T., Wang, H., Cui, L., & Liu, L. (2023). Evaluation of surface temperature and pressure derived from MERRA-2 and ERA5 reanalysis datasets and their applications in hourly GNSS precipitable water vapor retrieval over China. *Geodesy and Geodynamics*, *14*(2), 111–120. https://doi.org/10.1016/j.geog.2022.08.006

Inamdar, A. K., French, A., Hook, S., Vaughan, G., & Luckett, W. (2008). Land surface temperature retrieval at high spatial and temporal resolutions over the southwestern United States. *Journal of Geophysical Research: Atmospheres*, *113*(D7). https://doi.org/10.1029/2007JD009048

Jia, A., Liang, S., & Wang, D. (2022). Generating a 2-km, all-sky, hourly land surface temperature product from Advanced Baseline Imager data. *Remote Sensing of Environment*, *278*, 113105. https://doi.org/10.1016/j.rse.2022.113105

Jia, A., Liang, S., Wang, D., Ma, L., Wang, Z., & Xu, S. (2023). Global hourly, 5 km, all-sky land surface temperature data from 2011 to 2021 based on integrating geostationary and polar-orbiting satellite data. *Earth System Science Data*, *15*(2), 869–895. https://doi.org/10.5194/essd-15-869-2023

Jia, A., Liang, S., Wang, D., Mallick, K., Zhou, S., Hu, T., & Xu, S. (2024). Advances in Methodology and Generation of All-Weather Land Surface Temperature Products From

887 Polar-Orbiting and Geostationary Satellites: A comprehensive review. *IEEE Geoscience*
888 *and Remote Sensing Magazine*, *12*(4), 218–260. IEEE Geoscience and Remote
889 Sensing Magazine. https://doi.org/10.1109/MGRS.2024.3421268
890 Jiang, Y., Kim, J. B., Trugman, A. T., Kim, Y., & Still, C. J. (2019). Linking tree physiological
891 constraints with predictions of carbon and water fluxes at an old-growth coniferous
892 forest. *Ecosphere*, *10*(4), e02692. https://doi.org/10.1002/ecs2.2692
893 Jin, M., & Liang, S. (2006). An Improved Land Surface Emissivity Parameter for Land Surface
894 Models Using Global Remote Sensing Observations. *Journal of Climate*, *19*(12), 2867–
895 2881. https://doi.org/10.1175/JCLI3720.1
896 Kalma, J. D., McVicar, T. R., & McCabe, M. F. (2008). Estimating Land Surface Evaporation: A
897 Review of Methods Using Remotely Sensed Surface Temperature Data. *Surveys in*
898 *Geophysics*, *29*(4), 421–469. https://doi.org/10.1007/s10712-008-9037-z
899 Karnieli, A., Agam, N., Pinker, R. T., Anderson, M., Imhoff, M. L., Gutman, G. G., Panov, N., &
900 Goldberg, A. (2010). *Use of NDVI and Land Surface Temperature for Drought*
901 *Assessment: Merits and Limitations*. https://doi.org/10.1175/2009JCLI2900.1
902 Koster, R. D., Reichle, R. H., Mahanama, S. P. P., Perket, J., Liu, Q., & Partyka, G. (2020).
903 Land-Focused Changes in the Updated GEOS FP System (Version 5.25). *GMAO*
904 *Research Brief*. https://gmao.gsfc.nasa.gov/researchbriefs/land_changes_GEOS-
905 FP/land_changes_GEOS-FP.pdf
906 Koster, R. D., Suarez, M. J., Ducharne, A., Stieglitz, M., & Kumar, P. (2000). A catchment-
907 based approach to modeling land surface processes in a general circulation model: 1.
908 Model structure. *Journal of Geophysical Research: Atmospheres*, *105*(D20), 24809–
909 24822. https://doi.org/10.1029/2000JD900327
910 Kuenzer, C., & Dech, S. (2013). Theoretical Background of Thermal Infrared Remote Sensing.
911 In C. Kuenzer & S. Dech (Eds.), *Thermal Infrared Remote Sensing: Sensors, Methods,*

Applications (pp. 1–26). Springer Netherlands. https://doi.org/10.1007/978-94-007-6639-6_1

Lagouarde, J.-P., Ballans, H., Moreau, P., Guyon, D., & Coraboeuf, D. (2000). Experimental Study of Brightness Surface Temperature Angular Variations of Maritime Pine (*Pinus pinaster*) Stands. *Remote Sensing of Environment*, *72*(1), 17–34. https://doi.org/10.1016/S0034-4257(99)00085-1

Li, L., Yang, Z.-L., Matheny, A. M., Zheng, H., Swenson, S. C., Lawrence, D. M., Barlage, M., Yan, B., McDowell, N. G., & Leung, L. R. (2021). Representation of Plant Hydraulics in the Noah-MP Land Surface Model: Model Development and Multiscale Evaluation. *Journal of Advances in Modeling Earth Systems*, *13*(4), e2020MS002214. https://doi.org/10.1029/2020MS002214

Li, Z.-L., Wu, H., Duan, S.-B., Zhao, W., Ren, H., Liu, X., Leng, P., Tang, R., Ye, X., Zhu, J., Sun, Y., Si, M., Liu, M., Li, J., Zhang, X., Shang, G., Tang, B.-H., Yan, G., & Zhou, C. (2023). Satellite Remote Sensing of Global Land Surface Temperature: Definition, Methods, Products, and Applications. *Reviews of Geophysics*, *61*(1), e2022RG000777. https://doi.org/10.1029/2022RG000777

Linderholm, H. W. (2006). Growing season changes in the last century. *Agricultural and Forest Meteorology*, *137*(1), 1–14. https://doi.org/10.1016/j.agrformet.2006.03.006

Lu, Y., Steele-Dunne, S. C., Farhadi, L., & van de Giesen, N. (2017). Mapping Surface Heat Fluxes by Assimilating SMAP Soil Moisture and GOES Land Surface Temperature Data. *Water Resources Research*, *53*(12), 10858–10877. https://doi.org/10.1002/2017WR021415

Ma, H., Zeng, J., Zhang, X., Fu, P., Zheng, D., Wigneron, J.-P., Chen, N., & Niyogi, D. (2021). Evaluation of six satellite- and model-based surface soil temperature datasets using global ground-based observations. *Remote Sensing of Environment*, *264*, 112605. https://doi.org/10.1016/j.rse.2021.112605

938 Meng, C. L., Li, Z.-L., Zhan, X., Shi, J. C., & Liu, C. Y. (2009). Land surface temperature data
939 assimilation and its impact on evapotranspiration estimates from the Common Land
940 Model. *Water Resources Research*, *45*(2). https://doi.org/10.1029/2008WR006971
941 Mira, M., Valor, E., Caselles, V., Rubio, E., Coll, C., Galve, J. M., Niclos, R., Sanchez, J. M., &
942 Boluda, R. (2010). Soil Moisture Effect on Thermal Infrared (8–13-μm) Emissivity. *IEEE*
943 *Transactions on Geoscience and Remote Sensing*, *48*(5), 2251–2260. IEEE
944 Transactions on Geoscience and Remote Sensing.
945 https://doi.org/10.1109/TGRS.2009.2039143
946 Müller, B., Bernhardt, M., Jackisch, C., & Schulz, K. (2016). Estimating spatially distributed soil
947 texture using time series of thermal remote sensing – a case study in central
948 Europe. *Hydrology and Earth System Sciences*, *20*(9), 3765–3775.
949 https://doi.org/10.5194/hess-20-3765-2016
950 Myneni, R., Knyazikhin, Y., & Park, T. (2021). *MODIS/Terra+Aqua Leaf Area Index/FPAR 8-Day*
951 *L4 Global 500m SIN Grid V061* [Dataset]. NASA EOSDIS Land Processes Distributed
952 Active Archive Center. https://doi.org/10.5067/MODIS/MCD15A2H.061
953 Norman, J. M., & Becker, F. (1995). Terminology in thermal infrared remote sensing of natural
954 surfaces. *Agricultural and Forest Meteorology, Thermal Remote Sensing of the Energy*
955 *and Water Balance over Vegetation*, *77*(3), 153–166. https://doi.org/10.1016/0168-
956 1923(95)02259-Z
957 Ogawa, K., Schmugge, T., Jacob, F., & French, A. (2003). Estimation of land surface window
958 (8–12 μm) emissivity from multi-spectral thermal infrared remote sensing—A case study
959 in a part of Sahara Desert. *Geophysical Research Letters*, *30*(2).
960 https://doi.org/10.1029/2002GL016354
961 Olivera-Guerra, L.-E., Ottlé, C., Raoult, N., & Peylin, P. (2025). Assimilating ESA CCI land
962 surface temperature into the ORCHIDEE land surface model: Insights from a multi-site

963 study across Europe. *Hydrology and Earth System Sciences*, *29*(1), 261–290.
964 https://doi.org/10.5194/hess-29-261-2025
965 Peng, J., Ma, J., Liu, Q., Liu, Y., Hu, Y., Li, Y., & Yue, Y. (2018). Spatial-temporal change of
966 land surface temperature across 285 cities in China: An urban-rural contrast perspective.
967 *Science of The Total Environment*, *635*, 487–497.
968 https://doi.org/10.1016/j.scitotenv.2018.04.105
969 Pérez-Planells, L., Niclòs, R., Valor, E., & Göttsche, F.-M. (2022). Retrieval of Land Surface
970 Emissivities Over Partially Vegetated Surfaces From Satellite Data Using Radiative
971 Transfer Models. *IEEE Transactions on Geoscience and Remote Sensing*, *60*, 1–21.
972 https://doi.org/10.1109/TGRS.2022.3224639
973 Pestana, S., Chickadel, C. C., Harpold, A., Kostadinov, T. S., Pai, H., Tyler, S., Webster, C., &
974 Lundquist, J. D. (2019). Bias Correction of Airborne Thermal Infrared Observations Over
975 Forests Using Melting Snow. *Water Resources Research*, *55*(12), 11331–11343.
976 https://doi.org/10.1029/2019WR025699
977 Pestana, S. J., Chickadel, C. C., & Lundquist, J. D. (2024). Thermal infrared shadow-hiding in
978 GOES-R ABI imagery: Snow and forest temperature observations from the SnowEx
979 2020 Grand Mesa field campaign. *The Cryosphere*, *18*(5), 2257–2276.
980 https://doi.org/10.5194/tc-18-2257-2024
981 Polgar, C. A., & Primack, R. B. (2011). Leaf-out phenology of temperate woody plants: From
982 trees to ecosystems. *New Phytologist*, *191*(4), 926–941. https://doi.org/10.1111/j.1469-
983 8137.2011.03803.x
984 Pomeroy, J. W., Marks, D., Link, T., Ellis, C., Hardy, J., Rowlands, A., & Granger, R. (2009).
985 The impact of coniferous forest temperature on incoming longwave radiation to melting
986 snow. *Hydrological Processes*, *23*(17), 2513–2525. https://doi.org/10.1002/hyp.7325
987 Qin, B., Chen, S., Cao, B., Yu, Y., Yu, P., Na, Q., Hou, E., Li, D., Jia, K., Yang, Y., Hu, T., Bian,
988 Z., Li, H., Xiao, Q., & Liu, Q. (2025). Angular normalization of GOES-16 and GOES-17

land surface temperature over overlapping region using an extended time-evolving kernel-driven model. *Remote Sensing of Environment*, *318*, 114532. https://doi.org/10.1016/j.rse.2024.114532

Reichle, R., De Lannoy, G., Koster, R., Crow, W., Kimball, J., & Liu, Q. (2018). *SMAP L4 Global 9 km EASE-Grid Surface and Root Zone Soil Moisture Land Model Constants, Version 4* [Dataset]. NASA National Snow and Ice Data Center Distributed Active Archive Center. https://doi.org/10.5067/KGLC3UH4TMAQ

Reichle, R. H., Draper, C. S., Liu, Q., Girotto, M., Mahanama, S. P. P., Koster, R. D., & Lannoy, G. J. M. D. (2017a). *Assessment of MERRA-2 Land Surface Hydrology Estimates*. https://doi.org/10.1175/JCLI-D-16-0720.1

Reichle, R. H., Kumar, S. V., Mahanama, S. P., Koster, R. D., & Liu, Q. (2010). Assimilation of satellite-derived skin temperature observations into land surface models. *Journal of Hydrometeorology*, *11*(5), 1103–1122.

Reichle, R. H., Liu, Q., Koster, R. D., Draper, C. S., Mahanama, S. P. P., & Partyka, G. S. (2017b). Land Surface Precipitation in MERRA-2. *Journal of Climate*, *30*(5), 1643–1664. https://doi.org/10.1175/JCLI-D-16-0570.1

Richardson, A. D., Anderson, R. S., Arain, M. A., Barr, A. G., Bohrer, G., Chen, G., Chen, J. M., Ciais, P., Davis, K. J., Desai, A. R., Dietze, M. C., Dragoni, D., Garrity, S. R., Gough, C. M., Grant, R., Hollinger, D. Y., Margolis, H. A., McCaughey, H., Migliavacca, M., … Xue, Y. (2012). Terrestrial biosphere models need better representation of vegetation phenology: Results from the North American Carbon Program Site Synthesis. *Global Change Biology*, *18*(2), 566–584. https://doi.org/10.1111/j.1365-2486.2011.02562.x

Roberts, D. A., Ustin, S. L., Ogunjemiyo, S., Greenberg, J., Dobrowski, S. Z., Chen, J., & Hinckley, T. M. (2004). Spectral and Structural Measures of Northwest Forest Vegetation at Leaf to Landscape Scales. *Ecosystems*, *7*(5), 545–562. https://doi.org/10.1007/s10021-004-0144-5

Rutter, N., Essery, R., Baxter, R., Hancock, S., Horton, M., Huntley, B., Reid, T., & Woodward, J. (2023). Canopy Structure and Air Temperature Inversions Impact Simulation of Sub-Canopy Longwave Radiation in Snow-Covered Boreal Forests. *Journal of Geophysical Research: Atmospheres*, *128*(14), e2022JD037980. https://doi.org/10.1029/2022JD037980

Seemann, S. W., Borbas, E. E., Knuteson, R. O., Stephenson, G. R., & Huang, H.-L. (2008). Development of a Global Infrared Land Surface Emissivity Database for Application to Clear Sky Sounding Retrievals from Multispectral Satellite Radiance Measurements. *Journal of Applied Meteorology and Climatology*, *47*(1), 108–123. https://doi.org/10.1175/2007JAMC1590.1

Slater, J. A., Garvey, G., Johnston, C., Haase, J., Heady, B., Kroenung, G., & Little, J. (2006). The SRTM Data “Finishing” Process and Products. *Photogrammetric Engineering & Remote Sensing*, *72*(3), 237–247. https://doi.org/10.14358/PERS.72.3.237

Staebler, R. M., & Fitzjarrald, D. R. (2005). Measuring Canopy Structure and the Kinematics of Subcanopy Flows in Two Forests. *Journal of Applied Meteorology*, *44*(8), 1161–1179. https://doi.org/10.1175/JAM2265.1

Staff, S. (2020). Gridded Soil Survey Geographic (gSSURGO) Database for the Conterminous United States. *United States Department of Agriculture, Natural Resources Conservation Service*.

Still, C. J., Rastogi, B., Page, G. F. M., Griffith, D. M., Sibley, A., Schulze, M., Hawkins, L., Pau, S., Detto, M., & Helliker, B. R. (2021). Imaging canopy temperature: Shedding (thermal) light on ecosystem processes. *New Phytologist*, *230*(5), 1746–1753. https://doi.org/10.1111/nph.17321

Sun, D., & Pinker, R. T. (2004). Case study of soil moisture effect on land surface temperature retrieval. *IEEE Geoscience and Remote Sensing Letters*, *1*(2), 127–130. IEEE Geoscience and Remote Sensing Letters. https://doi.org/10.1109/LGRS.2004.824749

Ulivieri, C., & Cannizzaro, G. (1985). Land surface temperature retrievals from satellite measurements. *Acta Astronautica*, *12*(12), 977–985. https://doi.org/10.1016/0094-5765(85)90026-8

Wang, D.-C., Zhang, G.-L., Zhao, M.-S., Pan, X.-Z., Zhao, Y.-G., Li, D.-C., & Macmillan, B. (2015). Retrieval and Mapping of Soil Texture Based on Land Surface Diurnal Temperature Range Data from MODIS. *PLOS ONE*, *10*(6), e0129977. https://doi.org/10.1371/journal.pone.0129977

Wang, Y.-R., Hessen, D. O., Samset, B. H., & Stordal, F. (2022). Evaluating global and regional land warming trends in the past decades with both MODIS and ERA5-Land land surface temperature data. *Remote Sensing of Environment*, *280*, 113181. https://doi.org/10.1016/j.rse.2022.113181

Watson, K. (1975). Geologic applications of thermal infrared images. *Proceedings of the IEEE*, *63*(1), 128–137. Proceedings of the IEEE. https://doi.org/10.1109/PROC.1975.9712

Yu, Y., Privette, J. L., & Pinheiro, A. C. (2008). Evaluation of Split-Window Land Surface Temperature Algorithms for Generating Climate Data Records. *IEEE Transactions on Geoscience and Remote Sensing*, *46*(1), 179–192. IEEE Transactions on Geoscience and Remote Sensing. https://doi.org/10.1109/TGRS.2007.909097

Yu, Y., Tarpley, D., Privette, J. L., Flynn, L. E., Xu, H., Chen, M., Vinnikov, K. Y., Sun, D., & Tian, Y. (2012). Validation of GOES-R Satellite Land Surface Temperature Algorithm Using SURFRAD Ground Measurements and Statistical Estimates of Error Properties. *IEEE Transactions on Geoscience and Remote Sensing*, *50*(3), 704–713. IEEE Transactions on Geoscience and Remote Sensing. https://doi.org/10.1109/TGRS.2011.2162338

Yu, Y., Tarpley, D., Xu, H., & Chen, M. (2012). GOES-R Advanced Baseline Imager (ABI) Algorithm Theoretical Basis Document For Land Surface Temperature (Version 2.5). *Noaa Nesdis Center For Satellite Applications And Research*.

Yu, Y., & Yu, P. (2020). GOES-R Advanced Baseline Imager (ABI) Algorithm Theoretical Basis Document For Land Surface Temperature. *Noaa Nesdis Center For Satellite Applications And Research*.

Zakrzewska, A., Kopeć, D., Krajewski, K., & Charyton, J. (2022). Canopy temperatures of selected tree species growing in the forest and outside the forest using aerial thermal infrared (3.6–4.9 μm) data. *European Journal of Remote Sensing*, *55*(1), 313–325. https://doi.org/10.1080/22797254.2022.2062055

Zhang, X., Tarpley, D., & Sullivan, J. T. (2007). Diverse responses of vegetation phenology to a warming climate. *Geophysical Research Letters*, *34*(19). https://doi.org/10.1029/2007GL031447

Zhao, W., Wen, F., Wang, Q., Sanchez, N., & Piles, M. (2021). Seamless downscaling of the ESA CCI soil moisture data at the daily scale with MODIS land products. *Journal of Hydrology*, *603*, 126930. https://doi.org/10.1016/j.jhydrol.2021.126930

Zhu, P., & Burney, J. (2022). Untangling irrigation effects on maize water and heat stress alleviation using satellite data. *Hydrology and Earth System Sciences*, *26*(3), 827–840. https://doi.org/10.5194/hess-26-827-2022